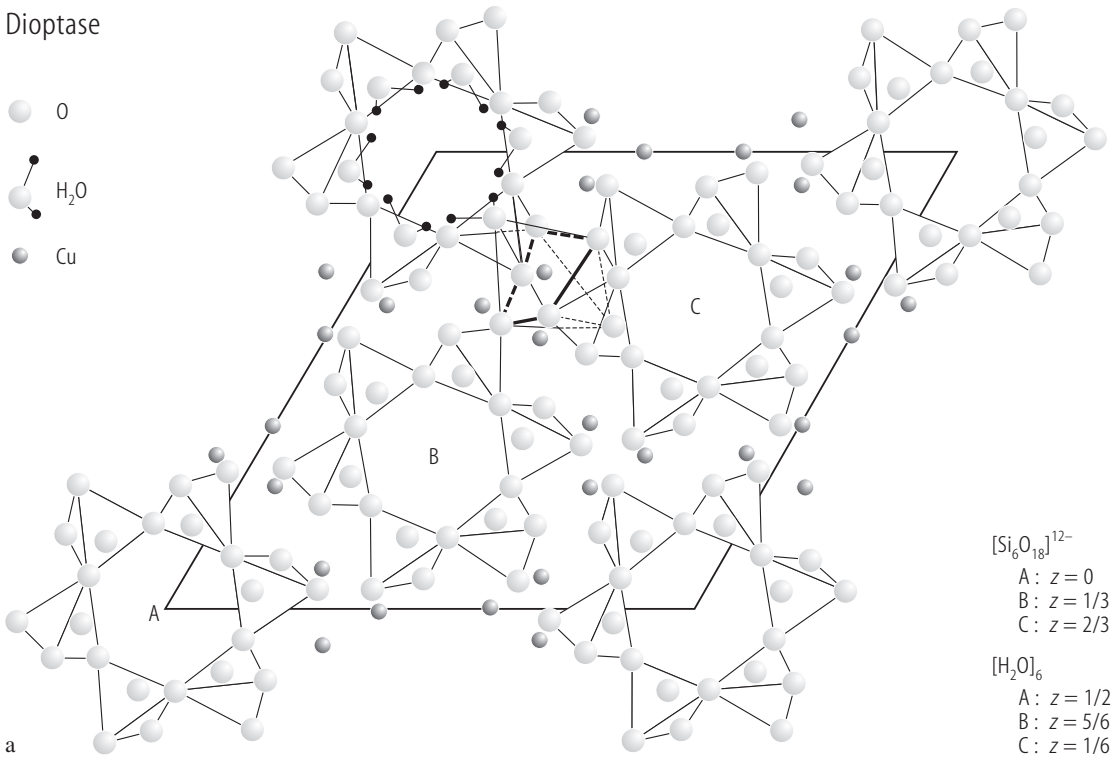

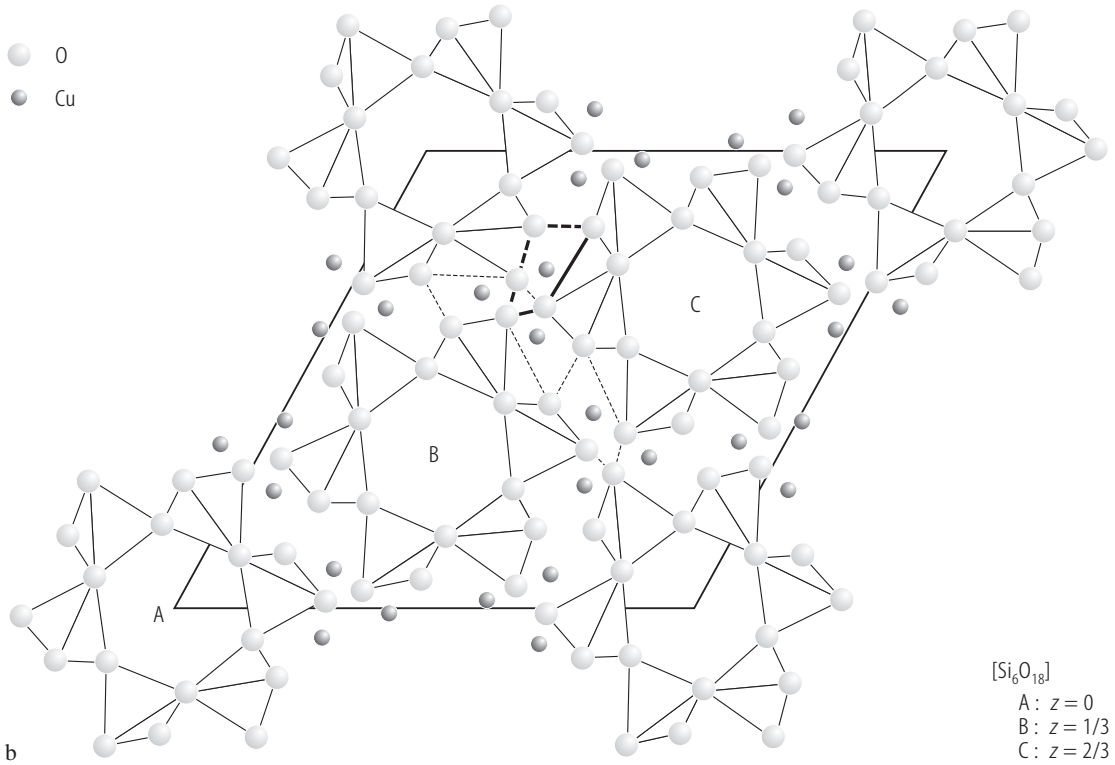

Fig. 1. Dioptase. Crystal structures: **(a)** green [77R1, 89B1]; **(b)** black [89B1].

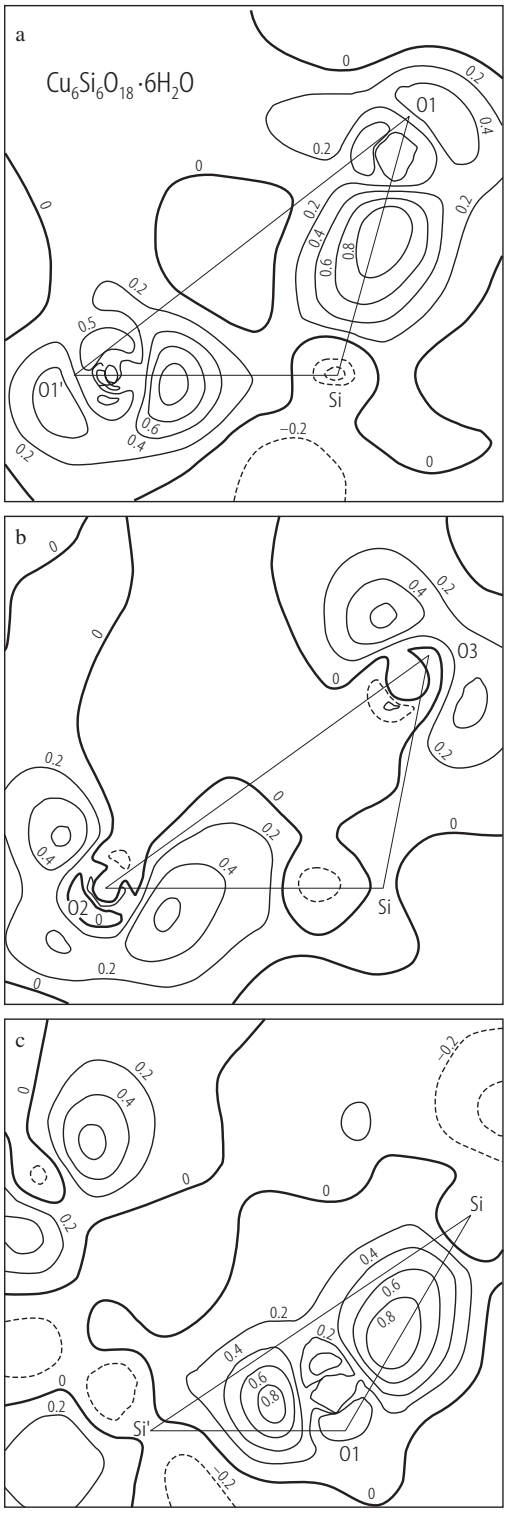

Fig. 2. $Cu_6Si_6O_{18}\cdot 6H_2O$. Static deformation density in SiO_4 tetrahedron sections: **(a)** O1-Si-O1'; **(b)** O2-Si-O3; **(c)** Si-O1-Si'. Contour interval is 0.2 eÅ^{-3}; zero level is given by bold, negative by dashed, and positive by solid lines [02B1].

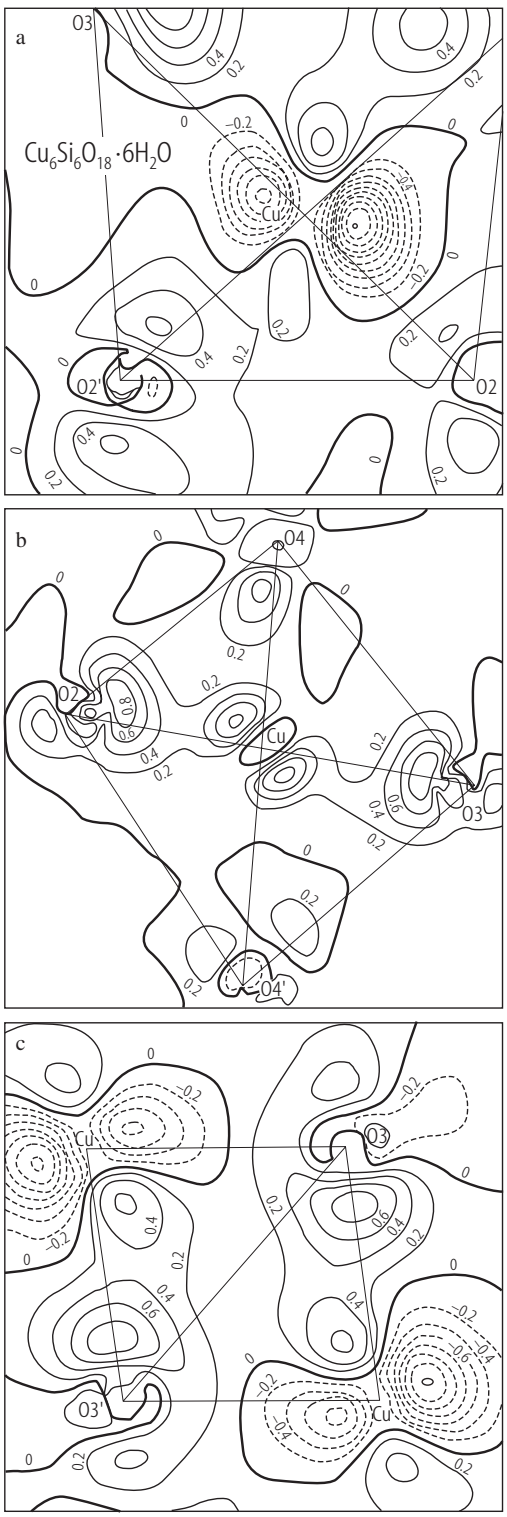

Fig. 3. $Cu_6Si_6O_{18}\cdot 6H_2O$. Static deformation density in Cu octahedron sections. (**a**) Via Cu, O2, O2', O3, O3', **(b)** combined from four triangles via the apical water molecule O4, O4', O2, and O3, **(c)** via Cu-Cu' pairs with common edge O3, O3' [02B1].

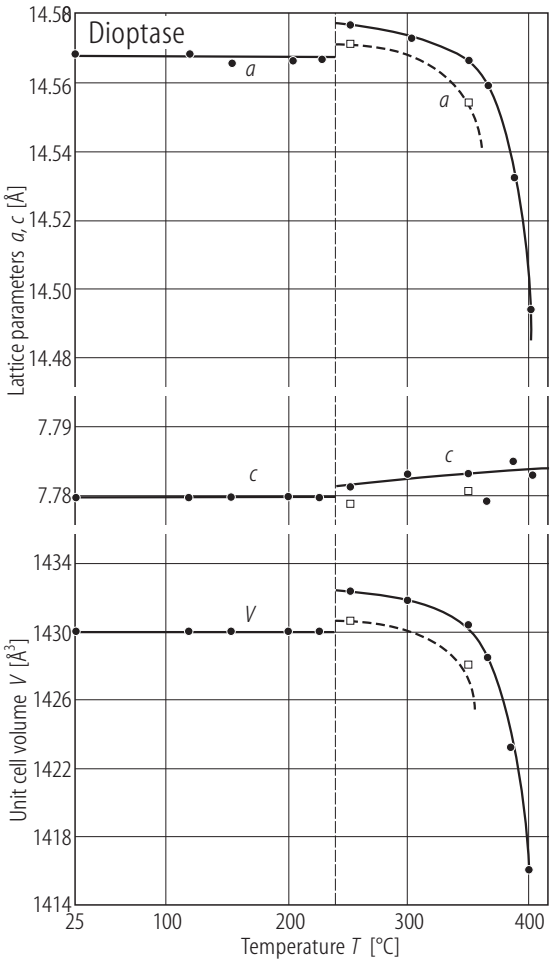

Fig. 4. Dioptase. Lattice parameters of hydrothermally annealed and quenched samples. Silicates kept for 2 days (dots) and 16 days (squares) at 0.5 kbar at various temperatures [88B1].

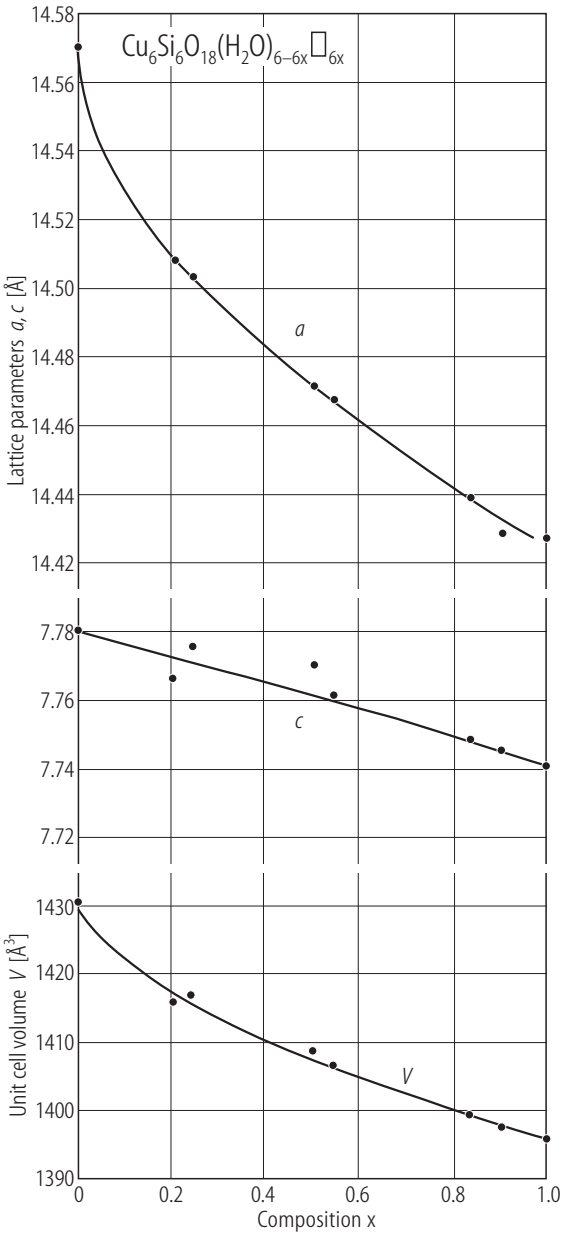

Fig. 5. $Cu_6Si_6O_{18}(H_2O)_{6-6x}\square_{6x}$. Lattice parameters as function of x, after annealing at 600°C in air [88B1].

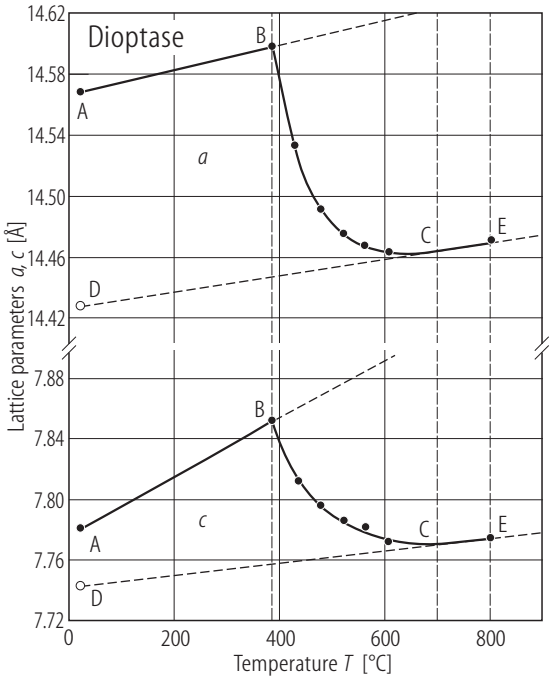

Fig. 6. Dioptase. Lattice parameters from a continuous high-temperature pattern starting with green dioptase (0.3°C/min). Black dioptase at room temperature A and D; B: begin of dehydration, C: end of dehydration; E: end of visible dioptase reflections [88B1].

For Fig. 7 see next page

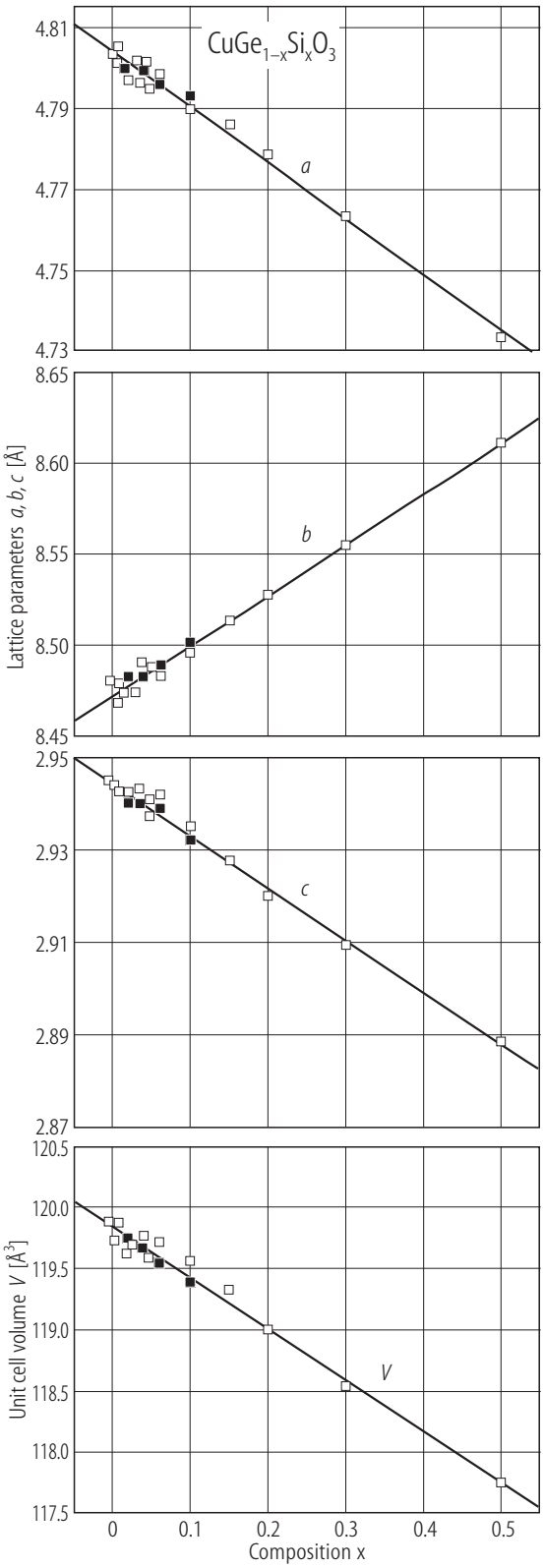

Fig. 8. $CuGe_{1-x}Si_xO_3$. Composition dependences of lattice parameters. The solid line represents a linear fit of the data. No difference between polycrystalline (□) and single crystal (■) samples was observed [97W1].

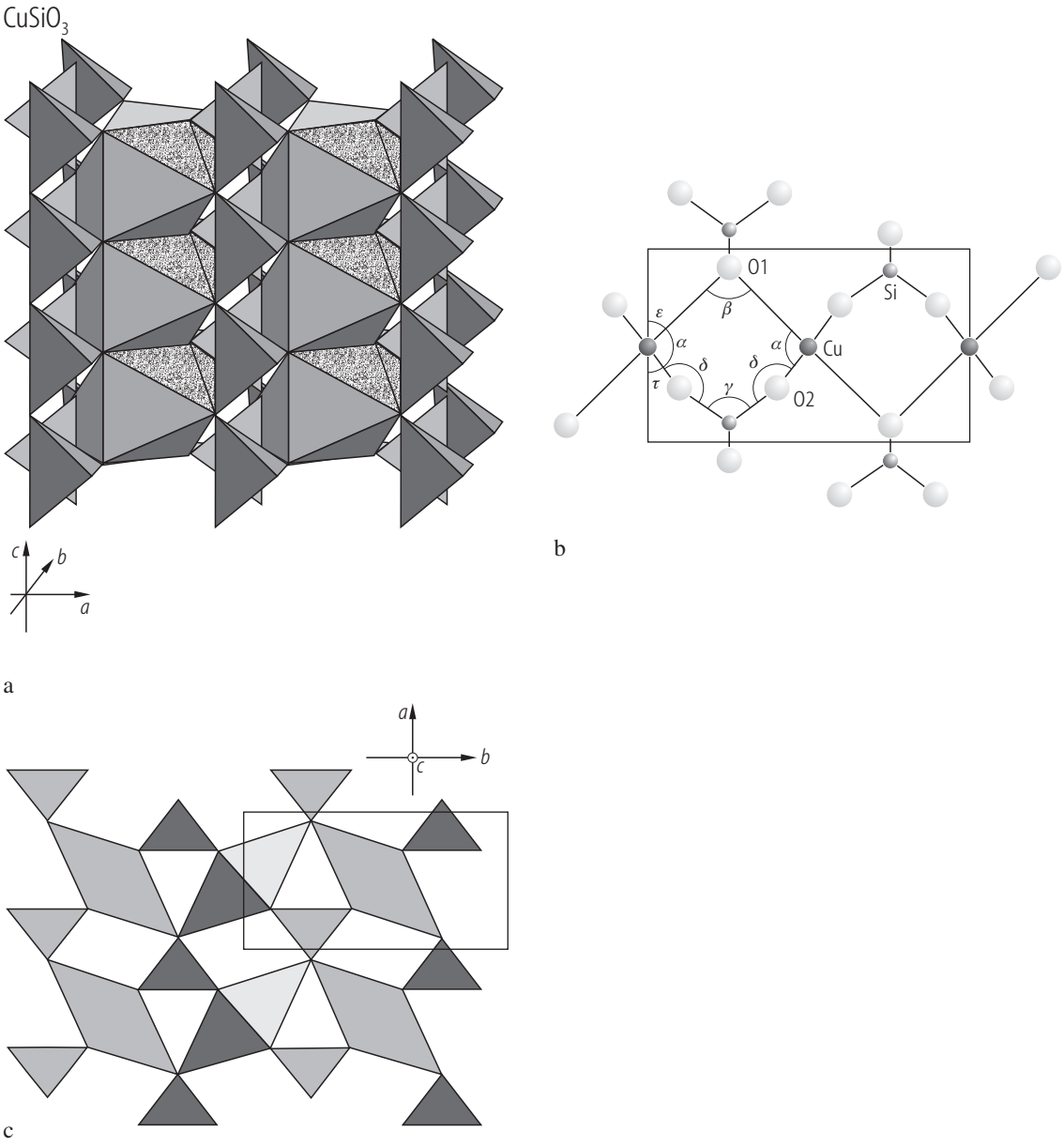

Fig. 7. $CuSiO_3$. **(a)** Picture of the crystal structure showing the connection of silicate and cuprate chains running down the ***c***-axis; **(b)** projection of the crystal structure along ***c*** [96B1, 98B1]; **(c)** polyhedra drawing of the crystal structure as projected down [001] showing the empty structural channels. The projected unit cell is outlined [04W1].

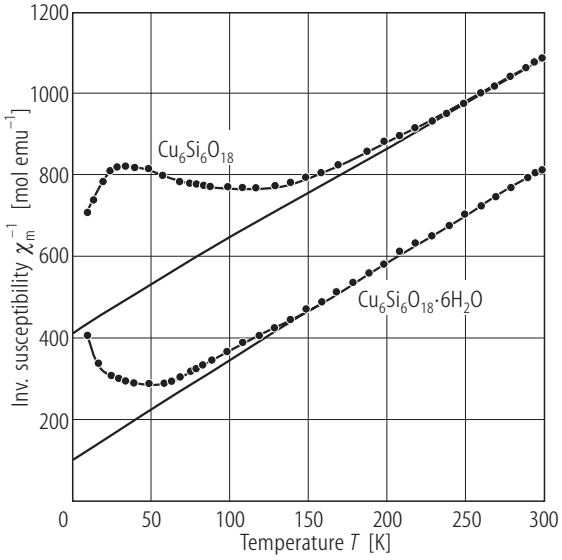

Fig. 9. $Cu_6Si_6O_{18}\cdot 6H_2O$ and $Cu_6Si_6O_{18}$. Thermal variations of inverse susceptibilities [93W1].

For Fig. 10 see next page

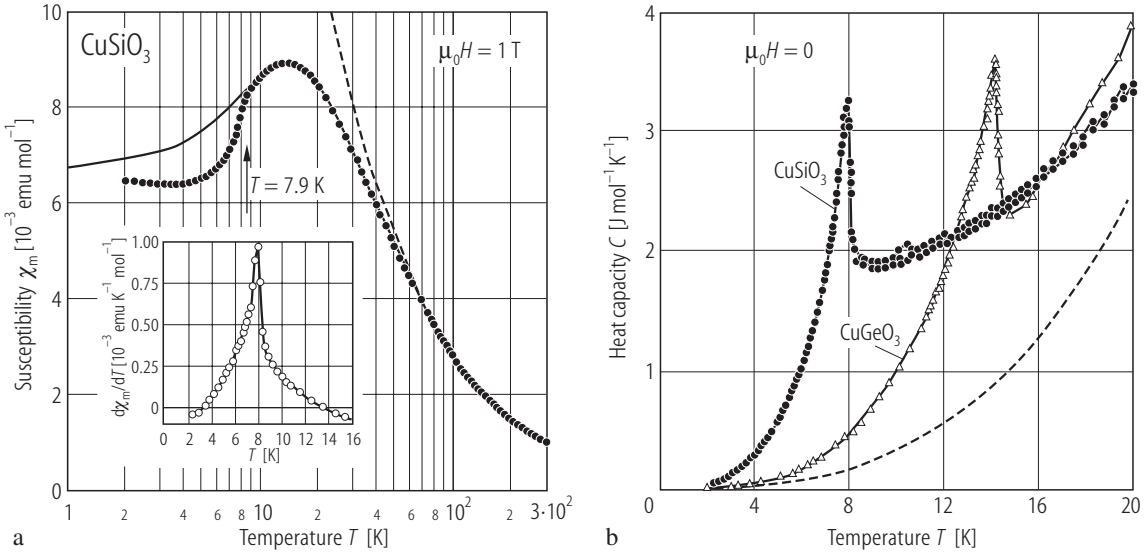

Fig. 11. $CuSiO_3$. **(a)** Temperature dependence of the magnetic susceptibility in a log T scale [00B1]. The solid curve corresponds to the numerical calculations for $S = ½$ 1D Heisenberg chains with nearest-neighbour coupling and without next-nearest neighbour coupling [98K1]. The fitting of the numerical results to the experimental $\chi_m(T)$ requires $J/k_B = 21$ K and an effective moment $p_{eff} = 1.60$ μ_B/Cu atom. At $T \geq 200$ K, $\chi_m(T)$ was fitted with a Curie-Weiss law (dashed line) with $p_{eff} = 1.56$ μ_B/Cu atom and $\Theta = -7.2$ K. The inset shows $d\chi_m/dT$ as function of temperature [00B1]. **(b)** Heat capacity of $CuMO_3$ for M = Ge [95L1] and Si [00B1]. The dashed line represents the phonon contribution $C_{ph} = \beta T^3$ for $CuGeO_3$ with $\beta = 0.32$ mJ/mol K^4.

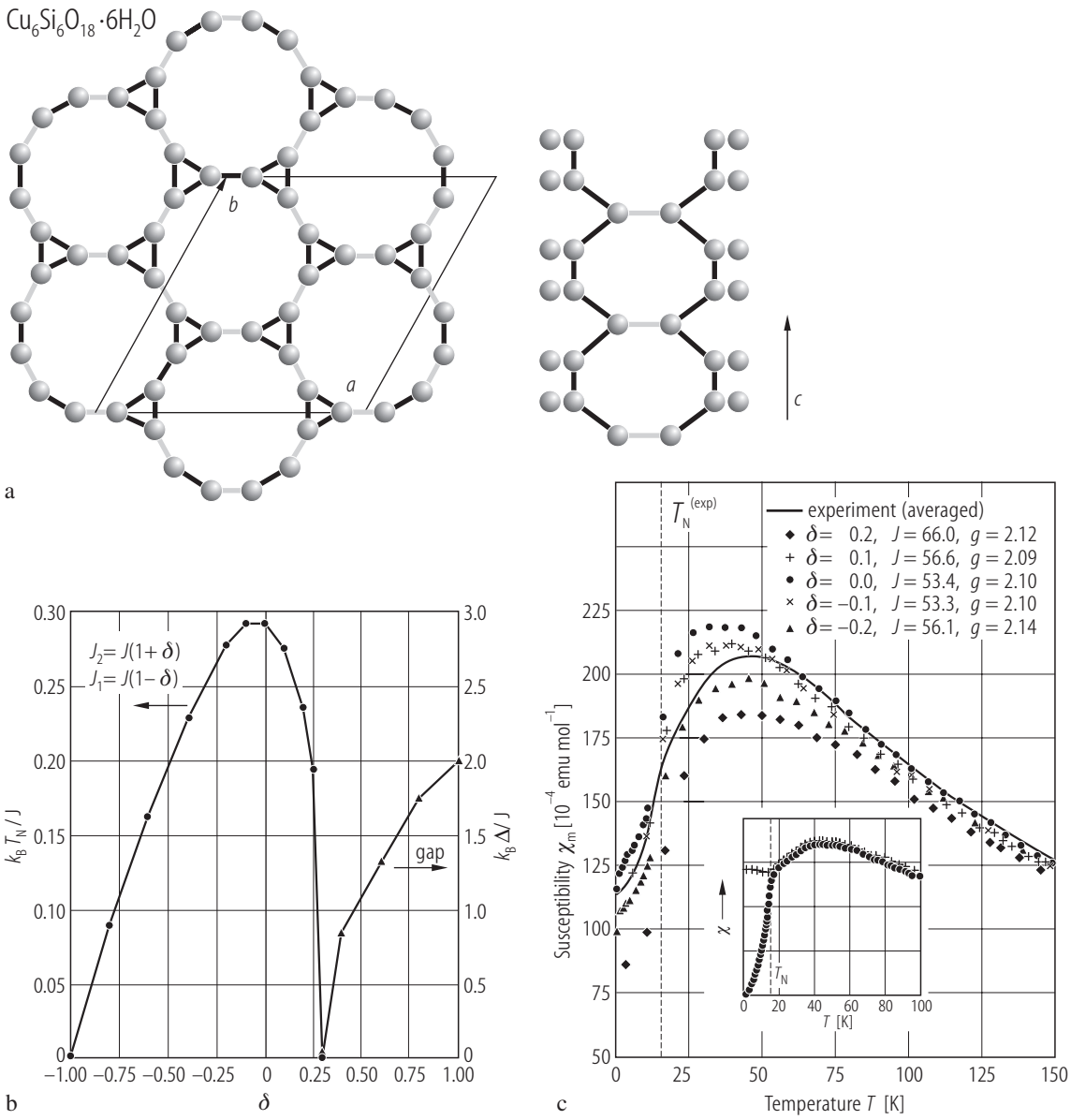

Fig. 10. $Cu_6Si_6O_{18}·6H_2O$. **(a)** Illustration of Cu-sublattice. The rhombohedral unit cell contains 18 equivalent Cu atoms arranged in six chains with three atoms down the ***c***-period. The inter/intra-chain magnetic couplings with strength J_2 and J_1 are indicated by white/black sticks. Left: an ***ab***-plane. Not shown are the Si_6O_{18} rings, located inside the 12-membered Cu rings. The rhombus denotes the in-plane hexagonal unit cell. Right: two chiral chains along ***c***. **(b)** Phase diagram of the magnetic sublattice as obtained by a Quantum Monte Carlo (QMC) simulation. At $\delta_c \cong 0.3$ a quantum phase transition occurs. The Néel temperature of the antiferromagnetically ordered phase, for $\delta < \delta_c$, is given by the left axis. The antiferromagnetic order is of AB type with doubling of the unit cell along ***c***. For $\delta > \delta_c$ a gap, given by the right axis, opens in the magnetic excitation spectrum and the state is a quantum spin liquid. **(c)** QMC results for the susceptibility for various δ values in comparison with the directional-averaged experimental susceptibility (solid line). Inset: the susceptibilities, χ, for magnetic fields parallel/orthogonal to the ***c***-axis (lower/upper) curve. The vertical dashed lines indicate the location of T_N [02G1].

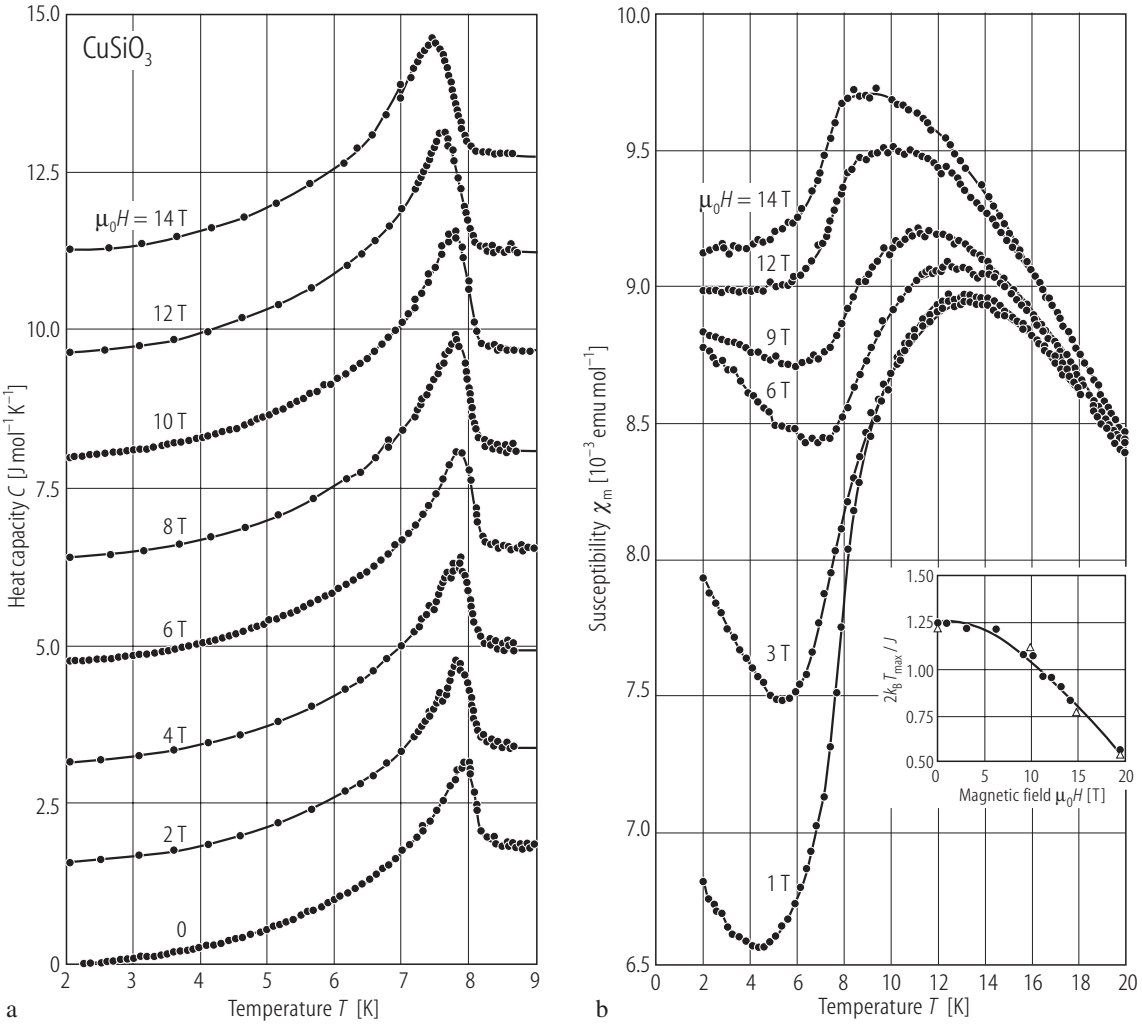

Fig. 12. $CuSiO_3$. **(a)** Temperature dependence of the heat capacity. The origin of the vertical axis was shifted by 1.6 J/mol K for the curves with $\mu_0 H \geq 0$. In **(b)** the magnetic susceptibilities were plotted at various fields as function of temperature [00B1]. The inset shows the shift of the temperature T_{max}, where the maxima in χ values were observed, in reduced units, as a function of applied field and in comparison with the theoretical prediction; triangles: [98K1]; circles: [00B1].

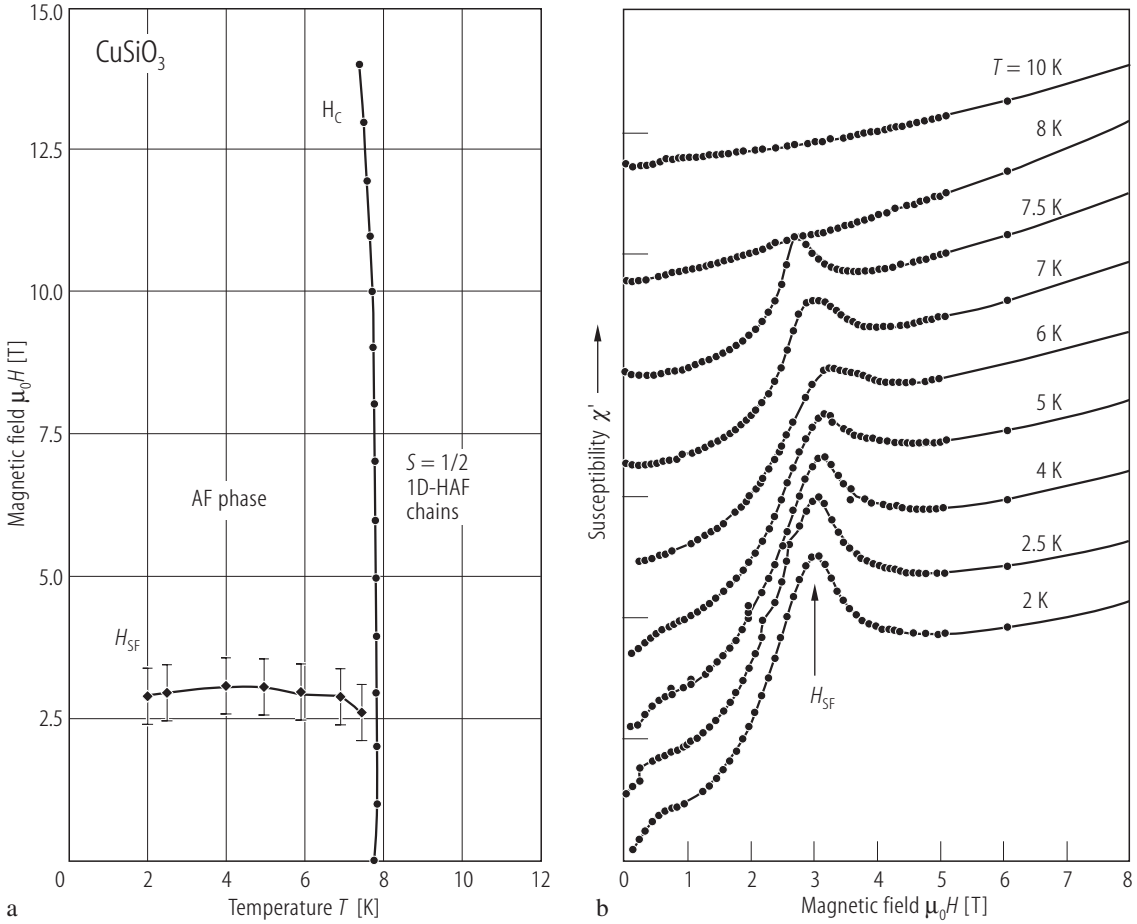

Fig. 13. $CuSiO_3$. Magnetic phase diagram **(a)** obtained from heat capacity and susceptibility measurements. H_c denotes the field for the AF transition and H_{SF} the field for the spin-flop transition as evidenced from ac-susceptibility measurements **(b).** The origin of the vertical scale was shifted by a constant value for curves obtained at different temperatures [00B1].

For Fig. 14 see next page

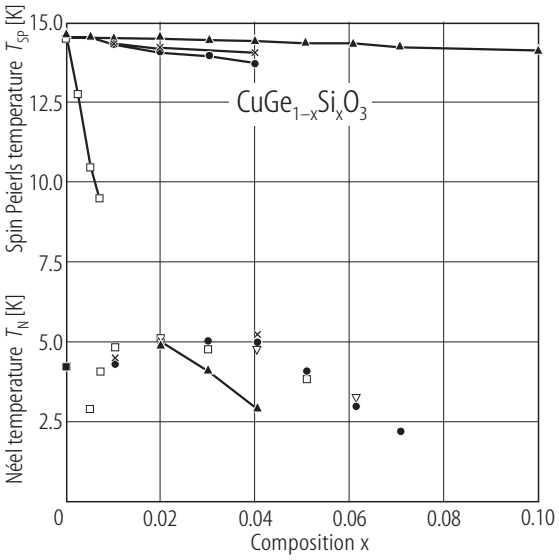

Fig. 15. $CuGe_{1-x}Si_xO_3$. Spin-Peierls (T_{SP})and Néel (T_N) temperatures as function of composition for single crystals (sc) and reduced and unreduced polycrystals (pc) [97W1]. Open squares: sc from [95R1], open triangle: flux-grown sc, full triangles: unreduced pc, crosses: lightly reduced pc, full circles: highly reduced pc, full squares: $CuGeO_{2.9}$.

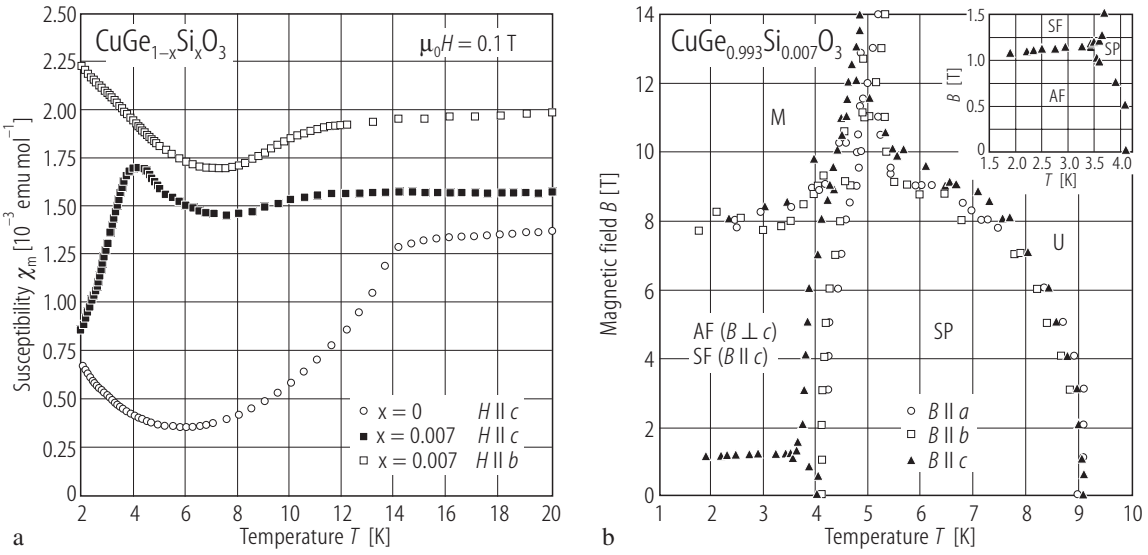

Fig. 14. $CuGe_{1-x}Si_xO_3$: **(a)** Magnetic susceptibilities as function of temperature for samples with x = 0 and 0.007 in a field of 0.1 T. **(b)** Magnetic phase diagram of a single crystal having x = 0.007 for magnetic fields oriented along the three orthorhombic axes. In inset, the bicritical point region is shown [95P1].

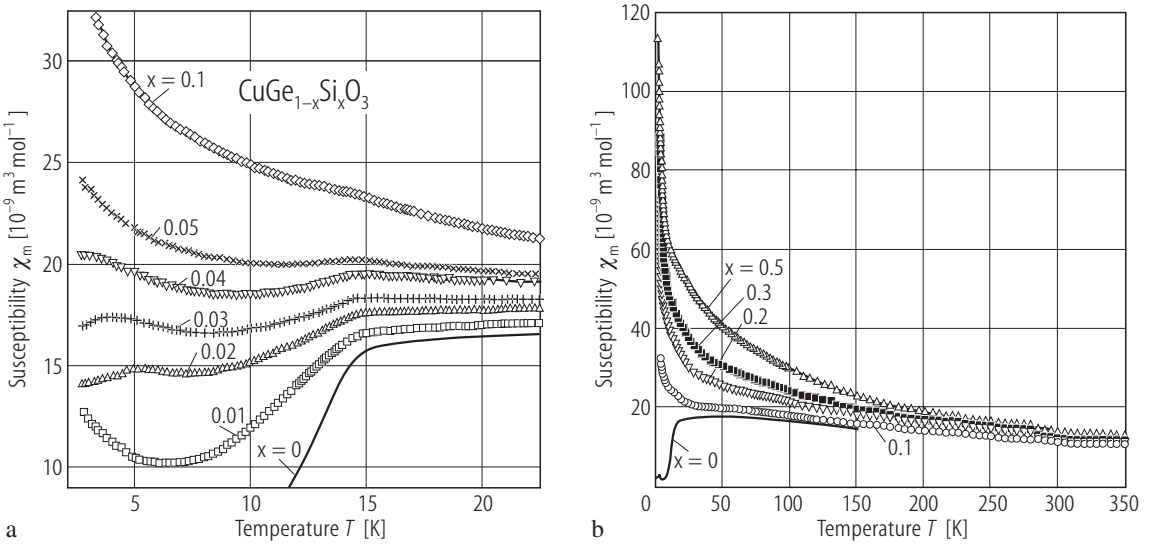

Fig. 16. $CuGe_{1-x}Si_xO_3$, polycrystalline samples. **(a)** Temperature dependences of the magnetic susceptibilities for x ≤ 0.1. The spin-Peierls transition is seen up to x = 0.1. T_{SP} remains nearly unchanged. The Néel transition appears at x = 0.02 (T_N = 5 K). T_N values decrease quite fast with increasing x down to 2.5 K for 4 at % Si. Both phase transitions coexist for 0.02 ≤ x ≤ 0.04 [97W1]. In **(b)** the temperature dependences of χ_m values for higher Si content than x = 0.1 are given [97W1]. With increasing Si content, the maximum at ≅ 56 K, characteristic of the one-dimensional behaviour, vanishes and is replaced by Curie-Weiss behaviour.

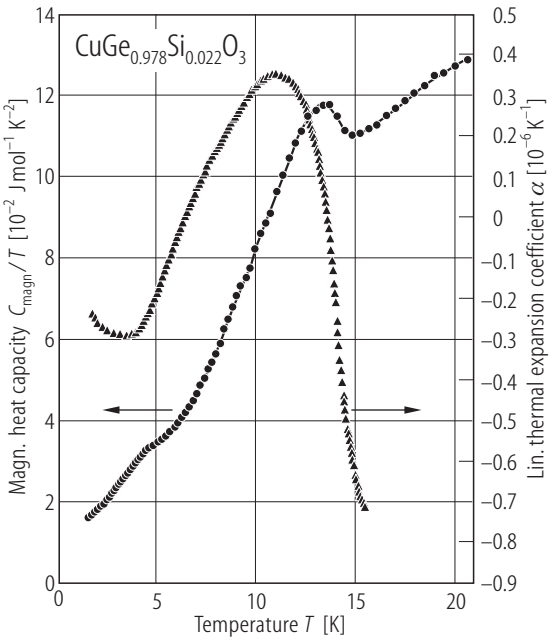

Fig. 17. $CuGe_{0.978}Si_{0.022}O_3$ polycrystal. Magnetic heat capacity (circles) and thermal expansion coefficient (triangles) as function of temperature [97W1].

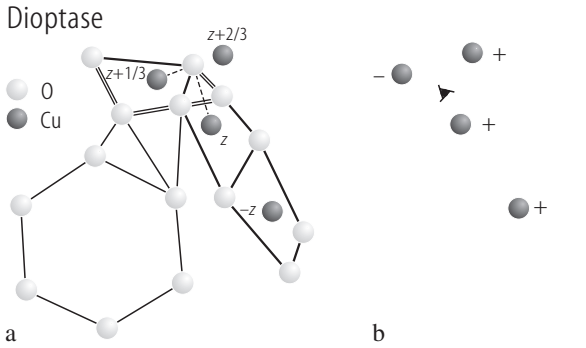

Fig. 18. Dioptase. The projection of a part of the unit cell of black dioptase onto the basal plane, showing the coordination of copper and the location of the silicate ring, $z_{Cu} = 0.0564$ **(a)**; its magnetic structure **(b)** [93W1].

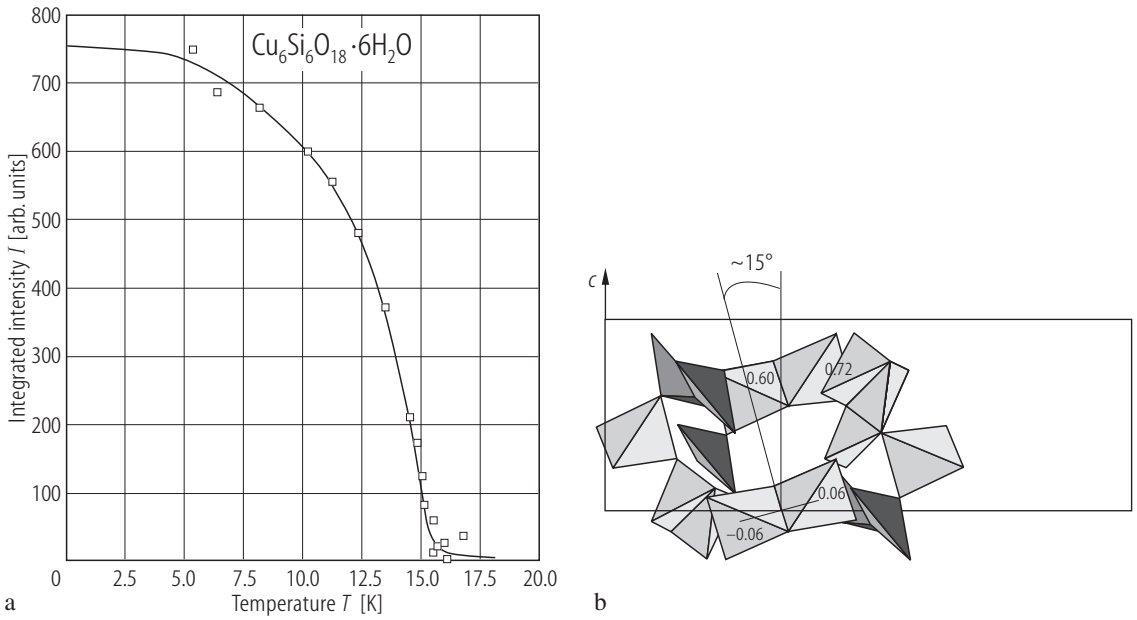

Fig. 19. Dioptase, $Cu_6Si_6O_{18}·6H_2O$. (**a**) Temperature dependence of the $(2,0,1/2)_{hex}$ reflection. **(b)** Fragment of the structure with triples of Cu squares at $z \cong 0$ and $z \cong 2/3$ along c_{hex}. The angle between the normal to the square and c_{hex} is shown [02B1].

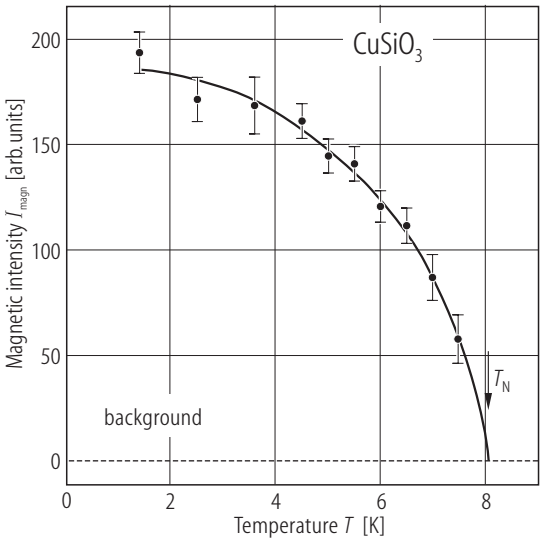

Fig. 20. $CuSiO_3$. Temperature dependence of the integrated magnetic neutron diffraction intensities, I_{magn}, for the (1/2, 1, –1/8) satellite [04W1].

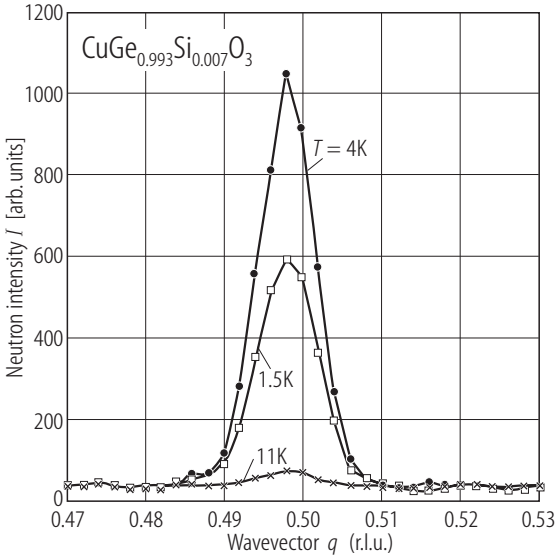

Fig. 21. $CuGe_{0.993}Si_{0.007}O_3$. Elastic neutron scattering scans around the dimerization peak (1/2,3,1/2) at 1.5 K ($T << T_N$), 4 K ($T \cong T_N$) and 11 K ($T > T_{SP}$). The persistence of the dimerization below the Néel temperature, T_N, of 3D-AF long-range order is observed [96R1].

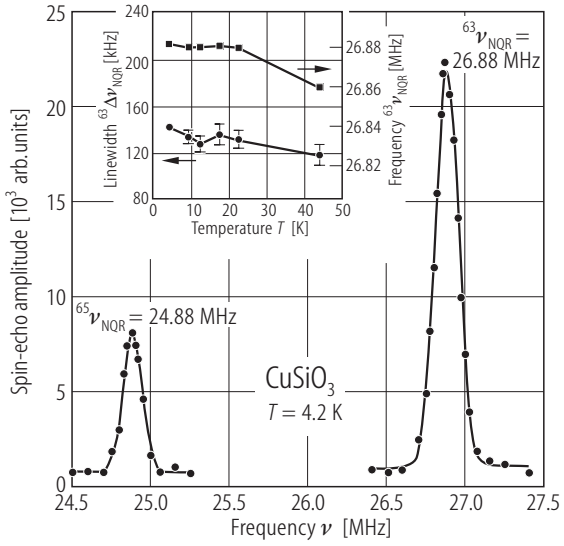

Fig. 22. $CuSiO_3$. ^{63}Cu and ^{65}Cu NQR spectra at 4.2 K. The solid curves correspond to the fitting of a Gaussian function to the experimental data. The inset shows the temperature dependence of the ^{63}Cu NQR frequency (right axis) and of the ^{63}Cu NQR linewidths (left axis) [00B1].

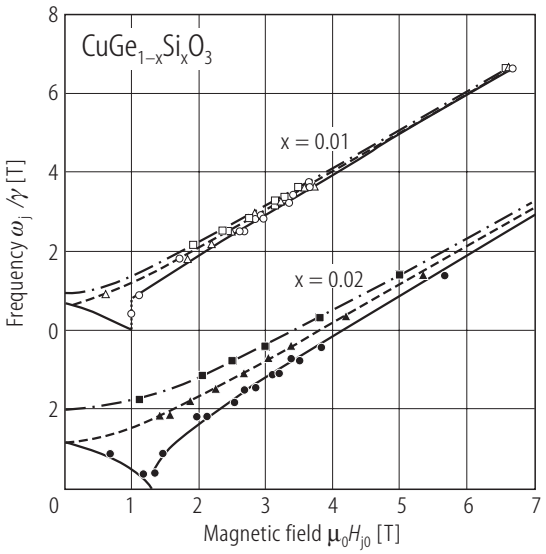

Fig. 23. $CuGe_{1-x}Si_xO_3$: AFMR frequency–field diagrams at 1.7 K for x = 0.01 and x = 0.02 samples [97N1]. Magnetic fields were applied along the ***a*** (open and full triangles), ***b*** (open and full squares) and ***c*** (open and full circles) axes, H_{j_o} (j = *a*, *b*, *c*) are the fields normalized by the *g* values, $H_{j_o} = g_j H/2$ (j = *a*, *b*, *c*).

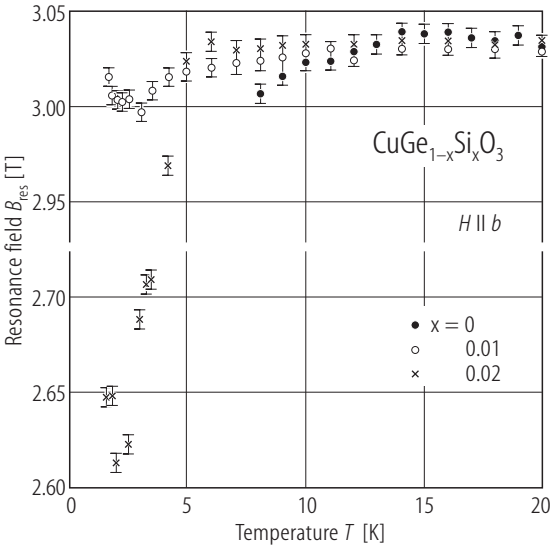

Fig. 24. $CuGe_{1-x}Si_xO_3$. Temperature dependences of the resonance field, B_{res}, at 95.5 GHz, for x = 0, 0.01 and 0.02 samples [97N1].

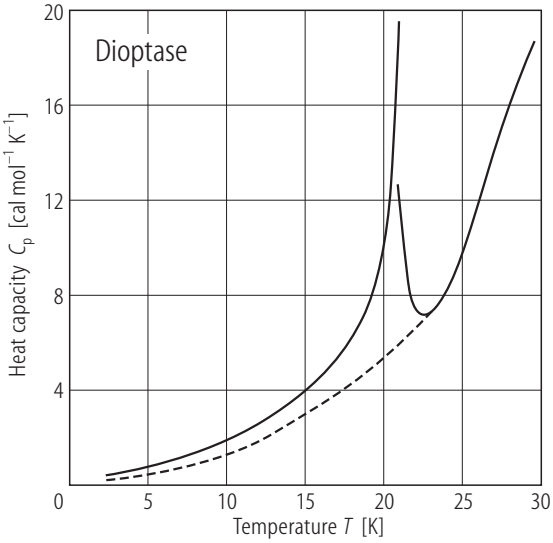

Fig. 25. Dioptase, $Cu_6Si_6O_{18}\cdot 6H_2O$. Temperature dependence of heat capacity. The dashed line is the lattice contribution [64E1].

For Fig. 26 see next page

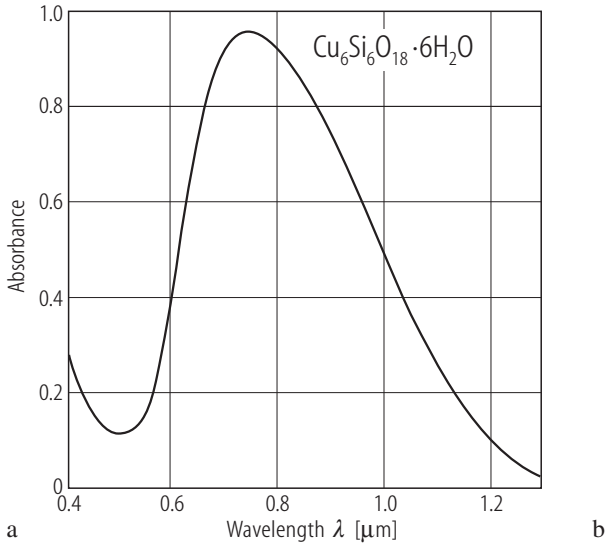

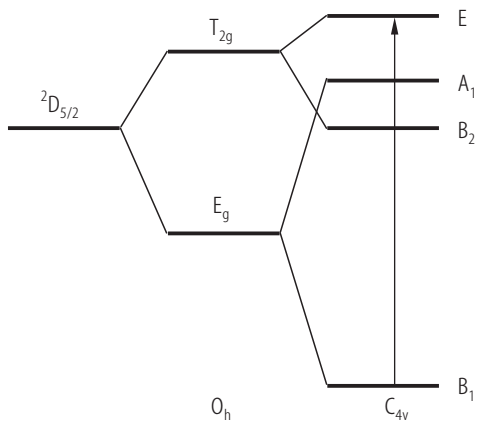

Fig. 27. Dioptase, $Cu_6Si_6O_{18}\cdot 6H_2O$. **(a)** Diffuse reflectance spectrum. **(b)** Energy level diagram for a d^9 ion in an octahedral field modified by a square planar distortion with $c > a$ [67N1].

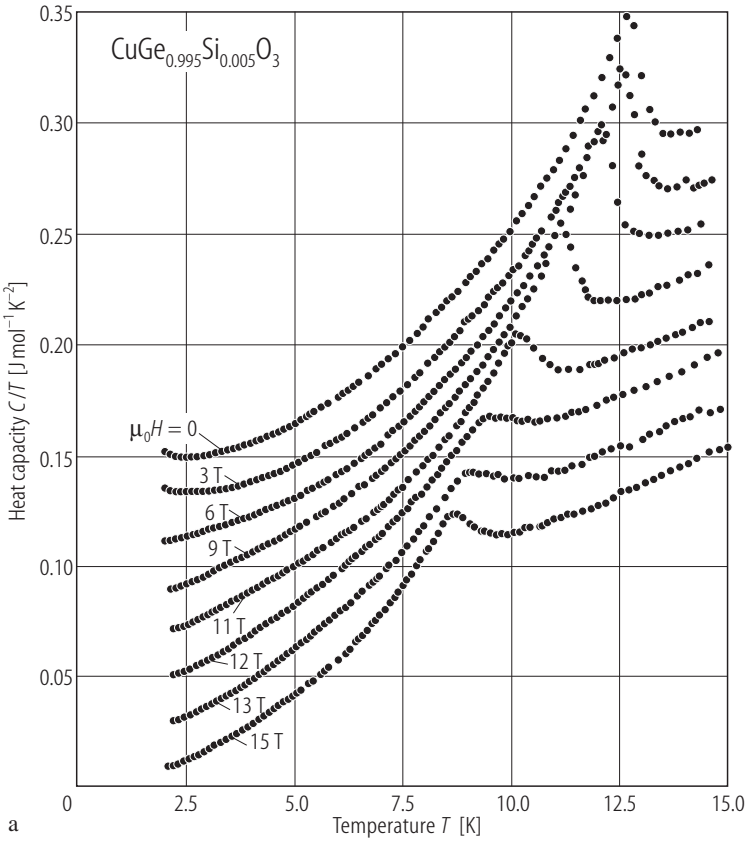

a

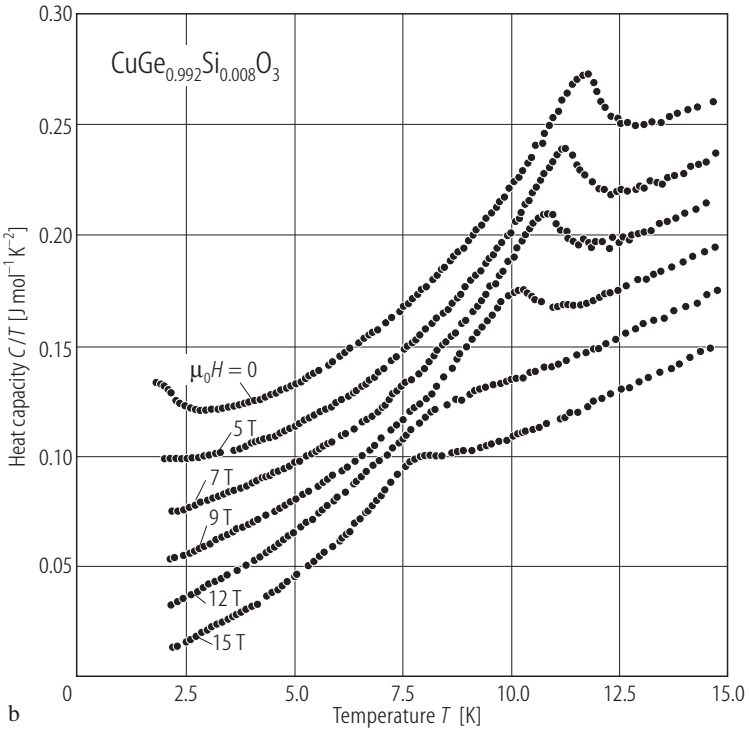

b

Fig. 26. $CuGe_{0.995}Si_{0.005}O_3$ **(a)**, $CuGe_{0.992}Si_{0.008}O_3$ **(b)**. Temperature dependences of the heat capacities under a magnetic field parallel to the ***a***-axis in the form C/T vs T. The origin of vertical axis is shifted by 0.02 J/mol K^2 [98H2].

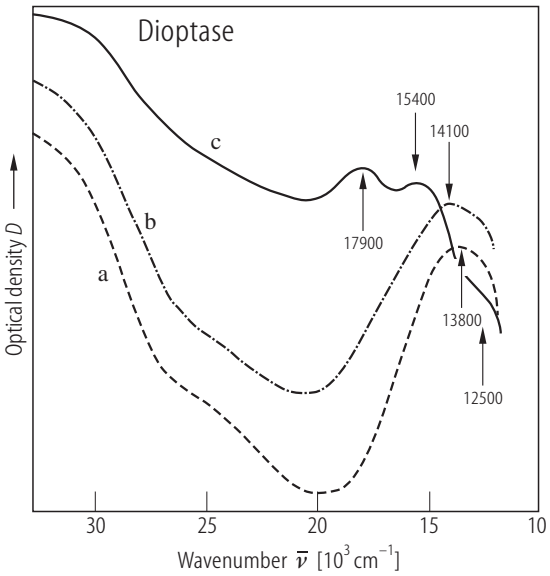

Fig. 28. Green (a), blue (b) and black (c) dioptase. Ligand field spectra (UV) [88B1].

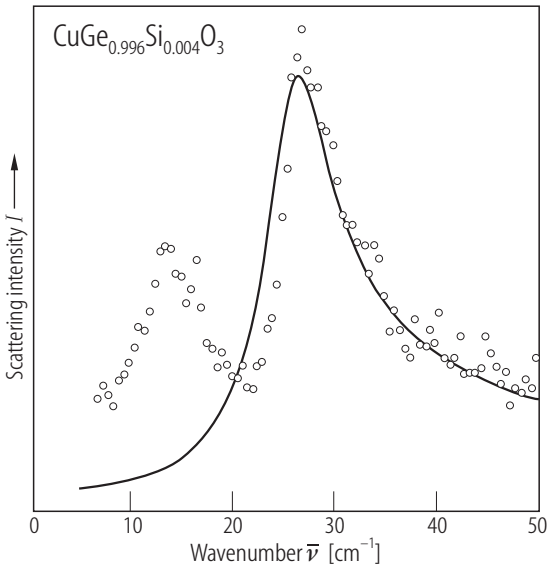

Fig. 32. $CuGe_{0.996}Si_{0.004}O_3$. Raman spectrum at 3 K. Solid curves denote the theory [98S1].

For Figs. 29, 31 see next pages

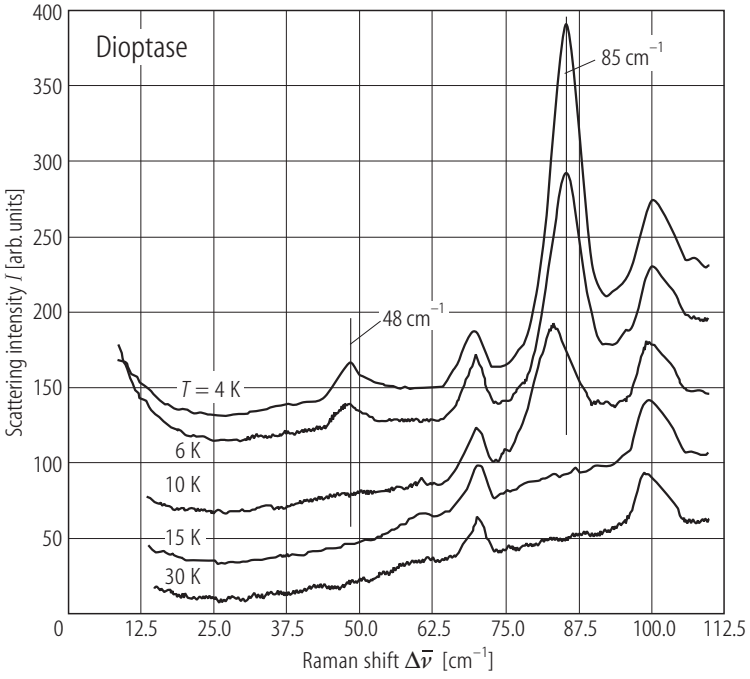

Fig. 30. Dioptase, $Cu_6Si_6O_{18}\cdot 6H_2O$. Low-energy Raman spectrum of green dioptase in *XX* polarization. The modes at 48 and 85 cm^{-1} (≅ 69 and 122 K) show a strong increase of intensity at $T < T_N$ and correspond to one- and two-magnon processes. The temperature-independent modes at 70 and 100 cm^{-1} are phonons [02G1].

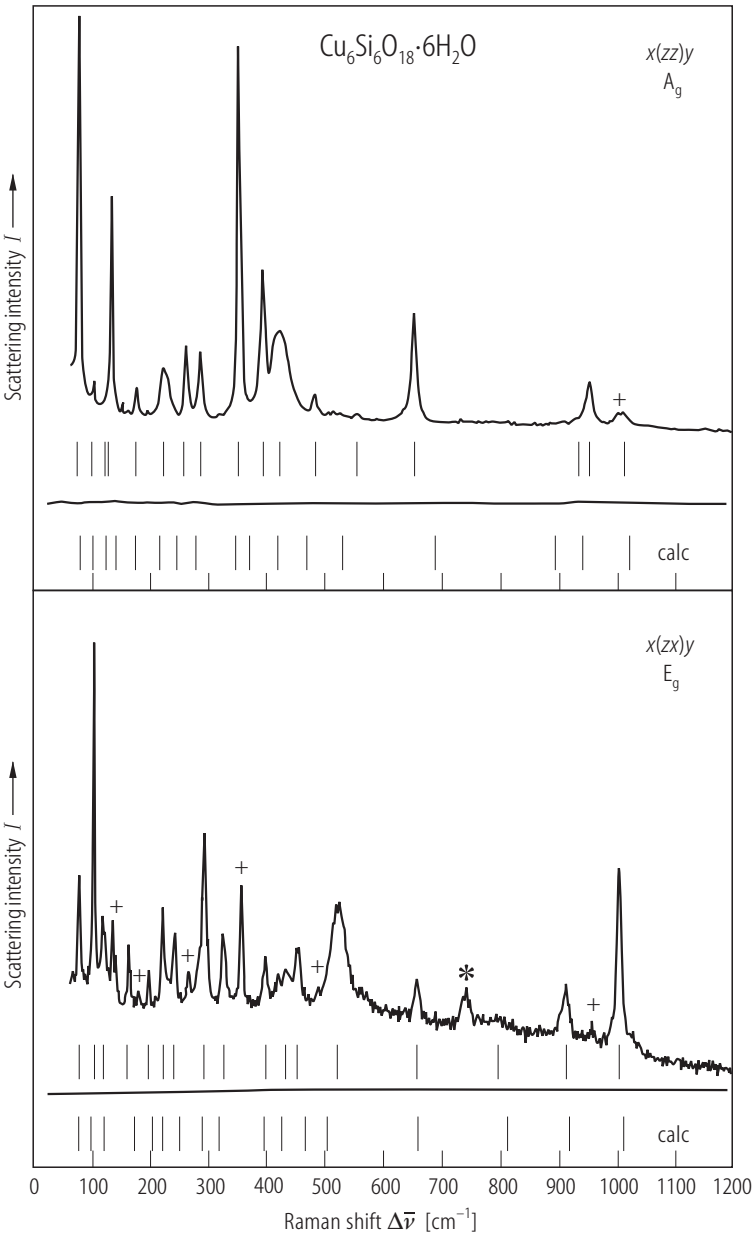

Fig. 29. Dioptase. $Cu_6Si_6O_{18}\cdot 6H_2O$. Raman spectra of A_g and E_g symmetries. Below, fundamental frequencies are indicated as vertical bars. By* is indicated a combination or overtone, and + indicates leakage from the other symmetry species. Labeled as calculated (calc), are the frequencies from the normal coordinate analysis plotted as vertical bars [95M1].

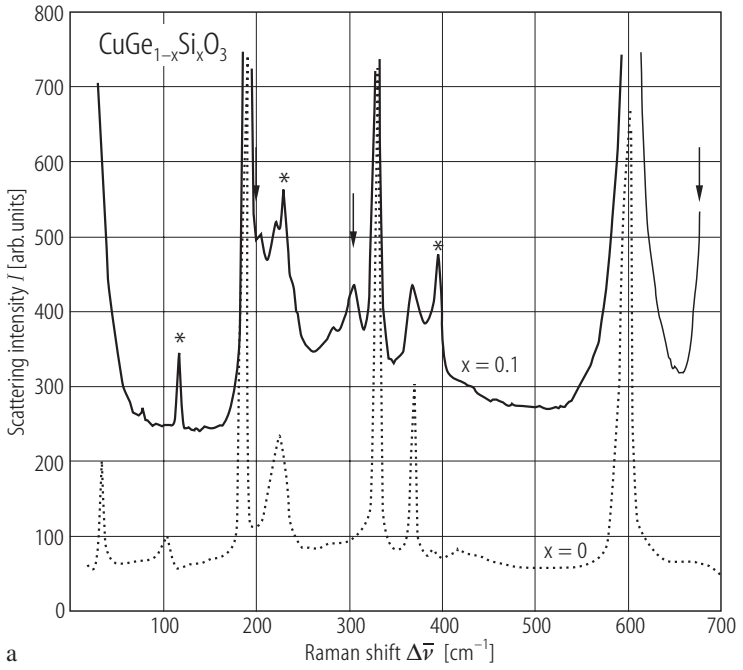

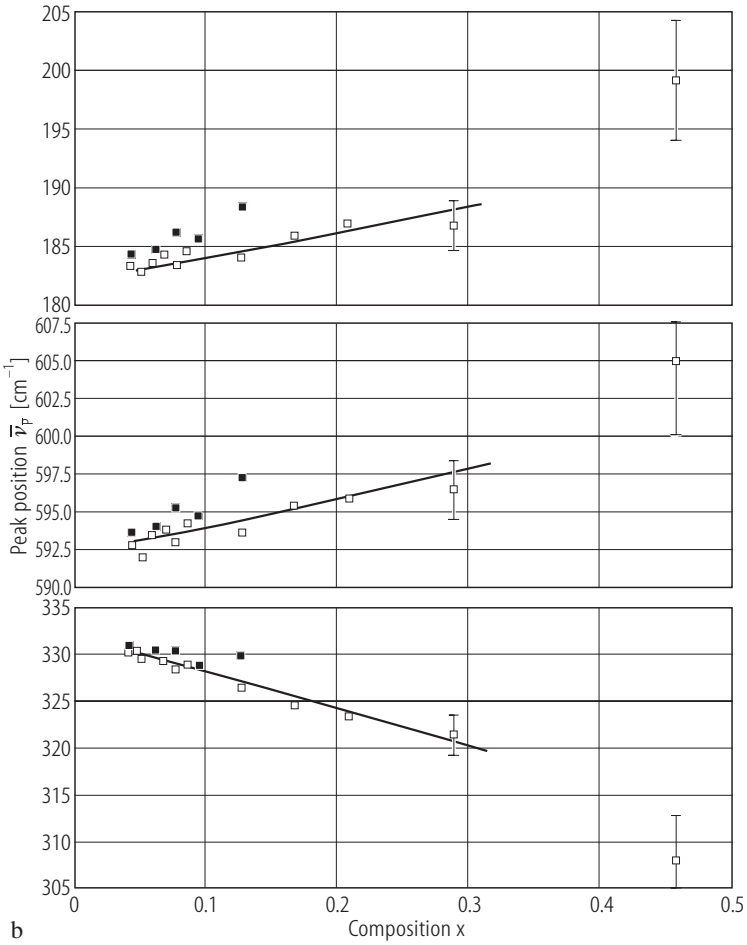

Fig. 31. $CuGe_{1-x}Si_xO_3$. **(a)** Normalized Raman-scattering intensity for compositions x = 0 and 0.1. The asterisks mark symmetry-forbidden phonon modes and the arrows defect modes induced by the substitution. **(b)** Some optical-phonon frequencies at room temperature vs composition. Linear composition dependences was shown up to x = 0.3. The other phonon frequencies which were not shown, remain unchanged. Solid symbols refer to sc's, open ones to pc samples. The sample with x = 0.5 shows a significant larger change of phonon frequency [97W1].